Multi-wavelength observations of the 2014 June 11 M3.9 flare: temporal and spatial characteristics

RAA 2019 Vol. **19** No. **7**, 101(10pp) doi: 10.1088/1674–4527/19/7/101

http://www.raa-journal.org *http://iopscience.iop.org/raa*

***R**esearch in*
***A**stronomy and*
***A**strophysics*

Multi-wavelength observations of the 2014 June 11 M3.9 flare: temporal and spatial characteristics

Damian J. Christian[1], David Kuridze[2,3], David B. Jess[3], Menoa Yousefi[1] and Mihalis Mathioudakis[3]

[1] Department of Physics and Astronomy, California State University Northridge, Northridge, CA 91330, USA; *damian.christian@csun.edu*

[2] Institute of Mathematics, Physics and Computer Science, Aberystwyth University, Ceredigion, Cymru, SY23 3, UK

[3] Astrophysics Research Center, School of Mathematics and Physics, Queen's University Belfast, Belfast BT7 INN, UK

Received 2018 November 17; accepted 2019 February 18

Abstract We present multi-wavelength observations of an M-class flare (M3.9) that occurred on 2014 June 11. Our observations were conducted with the Dunn Solar Telescope (DST), employing adaptive optics, the multi-camera system Rapid Oscillations in Solar Atmosphere (ROSA), the new Hydrogen-Alpha Rapid Dynamics camera (HARDcam) in various wavelengths, such as Ca II K, Mg I b_2 (at 5172.7 Å), and Hα narrow band and G-band continuum filters. Images were re-constructed using the Kiepenheuer-Institut Speckle Interferometry Package (KISIP) code, to improve our image resolution. We observed intensity increases of ≈120%–150% in the Mg, Ca K and Hα narrow band filters during the flare. Intensity increases for the flare observed in the *SDO* EUV channels were several times larger, and the X-rays, as recorded by *GOES*, increased over a factor of 30 for the harder band. Only a modest delay was found between the onset of flare ribbons of a nearby sympathetic flare and the main flare ribbons observed in these narrow band filters. The peak flare emission occurred within a few seconds for the Ca K, Mg and Hα bands. Time-distance techniques indicate propagation velocities of ≈60 km s^{-1} for the main flare ribbon and as high as 300 km s^{-1} for smaller regions, which we attribute to filament eruptions. This result and delays and velocities observed with *SDO* (≈100 km s^{-1}) for different coronal heights agree well with the simple model of energy propagation versus height, although a more detailed model for the flaring solar atmosphere is needed. Finally, we detected marginal quasi-periodic pulsations (QPPs) in the 40–60 s range for the Ca K, Mg and Hα bands, and such measurements are important for disentangling the detailed flare-physics.

Key words: magnetic reconnection — Sun: flares — Sun: atmosphere

1 INTRODUCTION

Solar flares vary in magnitude and frequency from rare, large, X-class flares, to common micro-flares and other sub-arcsecond explosive events (Jess et al. 2018). In flares, a rapid energy transfer occurs between the corona, chromosphere and photosphere through non-thermal electron beams, radiation, conduction, magnetoacoustic/Alfvén waves and mass motions. The intermittent nature of the non-thermal electron beams can result in very rapid variations in chromospheric and coronal emission. These variations arise from a combination of energy/ionization imbalance and chromospheric condensation, and are determined by the intensity of the non-thermal energy flux deposited in the lower atmosphere. The chromospheric plasma is heated to very high temperatures (5–30 MK) creating an overpressure, leading to an expansion into the overlying atmosphere. This in turn results in blueshifts in the upper chromosphere and transition region lines, a process known as chromospheric evaporation (Milligan et al. 2006; Pevtsov et al. 2007; Milligan 2015). On the other hand, due to the upward and downward momentum balance there should be a downflowing pattern (condensation) as a back-reaction to chromospheric evaporation, leading to redshifts of tens of kilometers per second in Hα (Kuridze et al. 2015). Additionally, many flares are accompanied by white light emission. White light flare emission is observed in

the near-ultraviolet (UV) and optical continuum, often appearing in transient footpoint regions (Neidig (1989); Isobe et al. (2007); Jess et al. (2008a), and see reviews by Hudson et al. (2006); Hudson (2011), for example). The energy content of the white light component of a flare may actually exceed the soft X-ray component by a factor of 100 (Hudson 2011).

There are many open questions on the conditions in the photosphere and chromosphere pre-flare, and their response during the flare. Recent advances in solar imaging in both spatial and temporal resolution allow us to measure the response of the photosphere and chromosphere at multiple heights in the solar atmosphere. Thus, the morphology and temporal changes of the flare emission observed in different narrow band filters (such as Ca K and Mg) promise to help constrain the detailed mechanisms of flare energy production and release, e.g. reviews by Fletcher et al. (2011); Hudson (2011). Lawrence et al. (1983), using observations in the Mg I b_2 line, found Mg flare kernels resembling white-light flare kernels, and associated the Mg emission with the impulsive flare phase. More recently, Bai et al. (2014) used Mg I b_2 to probe the poorly constrained chromospheric magnetic field.

In the present paper, we employ these new capabilities of higher spatial and temporal resolution from ground-based instrumentation and report on an M-class flare observed at several layers in the solar atmosphere. We examine an M3.9 flare observed on 2014 June 11 (SOL2014-06-11T21:03 UT), with the Rapid Oscillations of the Solar Atmosphere (ROSA), Hydrogen-Alpha Rapid Dynamics camera (HARDcam) and CSUNcam instruments at the National Solar Observatory's Dunn Solar Telescope (DST). In Section 2, we present the ROSA and ground-based observations and data analysis, and include observations from NASA's *Solar Dynamics Observatory* (*SDO*). In Section 3, we describe results for the flare characteristics, and compare these to previous observations, and discuss the flare propagation in simple models and search for quasi-periodic pulsations (QPPs) in Section 4. Lastly, in Section 5 we summarize our findings.

2 OBSERVATIONS

Our data were obtained with the ROSA (Jess et al. 2010) camera system. ROSA is a synchronized, multi-camera high cadence solar imager installed on the DST at the National Solar Observatory, Sacramento Peak, NM. The DST pointing was at S18.5E60.0, covering AR 12087 (at heliocentric coordinates, $-755''$, $-295''$). The observation sequence started at 19:20 UT and continued until 21:31 UT, with a span of just over 2 h and 11 min. The ROSA continuum channels recorded at 30 fps and images taken with the narrow band Mg I b_2 filter were acquired at half of this data rate. The ROSA set-up enabled a wider field of view than many previous studies, $\approx 2'$, giving a resolution of $0.12''$ per pixel or a 2-pixel diffraction-limited resolution of $\approx$173 km. ROSA was combined with the HARDcam (Jess et al. 2012) and CSUNcam (Grant et al. 2015), using Hα and Ca II K (hereafter Ca K) filters at a frame rate of 30 fps, respectively. Central wavelengths and filter properties for Hα and Ca K are given in Jess et al. (2010). Interferometric BIdimensional Spectrometer (Cavallini 2006; Reardon & Cavallini 2008) observations utilizing the Na D_1 line were also obtained and have been presented by Kuridze et al. (2016). The observations were recorded with high-order adaptive optics (Rimmele 2004) to correct wavefront deformations in real-time. Although the overall seeing was poor at times and the observations were hampered by clouds, we were able to measure the flare properties and perform speckle image reconstruction. The Kiepenheuer-Institut Speckle Interferometry Package (KISIP) speckle reconstruction algorithm (Wöger et al. 2008) was applied to the images, with a 64 to 1 restoration. The Mg I b_2 (hereafter Mg) data were acquired with a cadence of 15.15 fps, and the reconstructed cadence is 4.22 s per image. The Hα and Ca K data were obtained at 30.3 fps and both have a reconstructed cadence of 2.12 s per image. We searched for quasi-periodic fluctuations in our narrow band data employing wavelet techniques as described in Jess et al. (2008b). Our ground-based observations caught the M3.9 flare rising at $\sim$20:53 UT and peaking near 20:57 UT, and the *GOES* X-ray bands measured the flare peak at $\sim$21:03 UT. We show a sequence of flare images in the Ca K, Mg, Hα and G-band in Figure 1. Flare light curves for all three bands were extracted in a $34' \times 26'$ region.

2.1 *Solar Dynamics Observatory* Observations

We further supplemented our ROSA observations with extreme-ultraviolet (EUV) data from the Atmospheric Imaging Assembly (AIA) onboard the *SDO* (Lemen et al. 2012) and magnetic information from the Helioseismic and Magnetic Imager (HMI) (Scherrer et al. 2012; Schou et al. 2012). The AIA instrument images the entire solar disk in 10 different channels, incorporating a two-pixel spatial resolution of $1.2''$ ($\approx$900 km for the AIA's point spread function (PSF)) and a cadence of 12 s for the EUV channels and 24 s for the 1600 and 1700 Å channels. Here, we selected five EUV datasets spanning 20:30–22:00 UT from

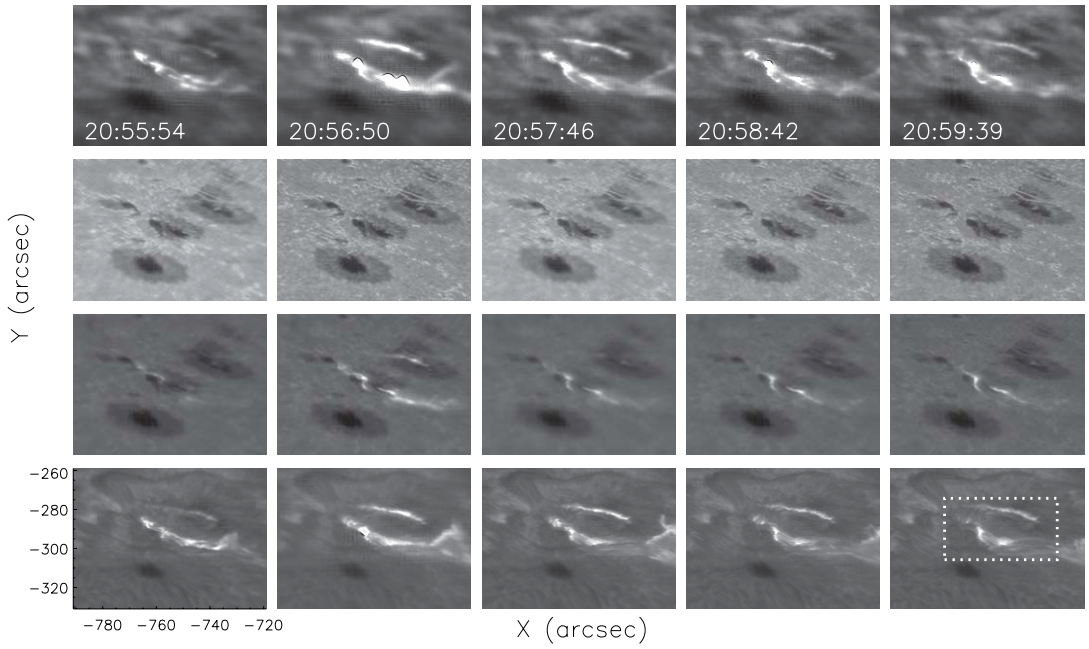

Fig. 1 Image sequence from ground-based observations acquired with ROSA, HARDcam and CSUNcam spanning the 2014 June 11 M3.9 class flare peak at intervals of about 1 min. Filters from top to bottom are: Ca K, G-band, Mg and Hα. The extraction region for flare light curves is indicated in the lower right panel for Hα.

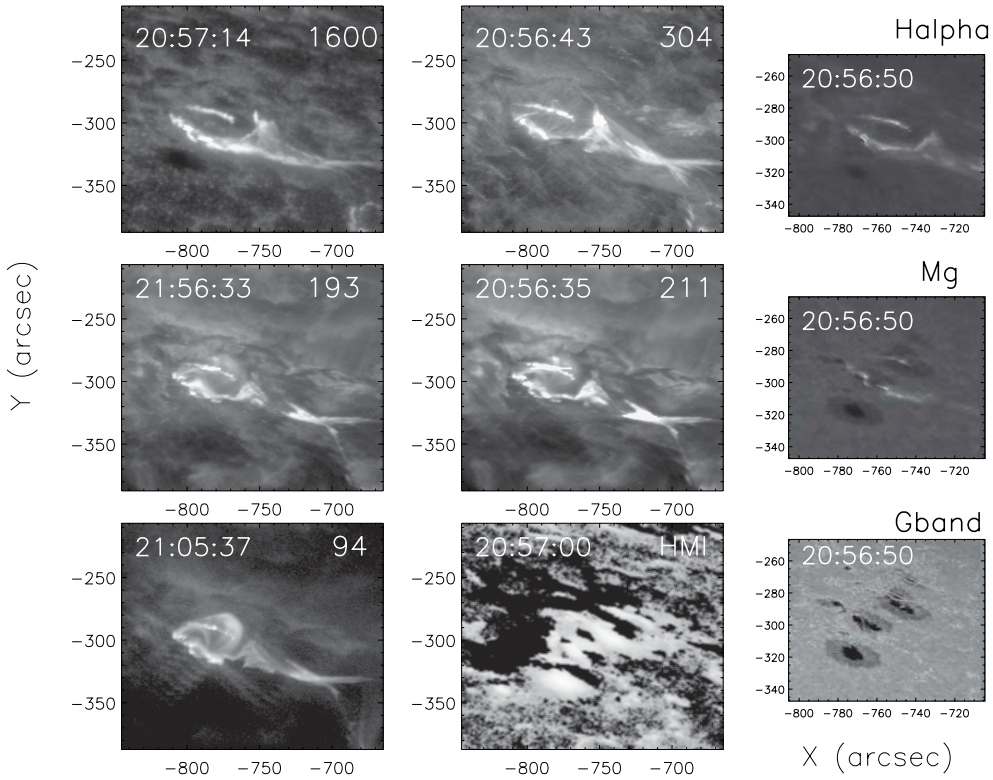

Fig. 2 *SDO*/AIA flare images in five different bands near the flare peak, along with our HARDCam Hα, ROSA G-band and Mg observations in the right column. The HMI LOS magnetogram is also shown in the lower middle panel (see text). (Note: Images were selected closest to the time of the flare peak in each band, but without saturation.)

2014 June 11, consisting of 445 images in each of the 94, 131, 193, 211, 304 and 335 Å AIA channels, and 222 images from the 1600 and 1700 Å channels. The *SDO* observations caught the M3.9 flare starting at approximately 20:53 UT and the subsequent brightening peaking near 20:57 for the cooler *SDO* channel and ∼21:06 UT for the hotter channels. The light curves from the different *SDO* channels were extracted in a $120'' \times 90''$ region. Sample *SDO* images along with our Mg and Hα bands are shown in Figure 2. We also obtained the HMI line-of-sight (LOS) magnetograms from 20:48 and 21:12 UT, before and after the flare, respectively. The HMI images were aligned and degraded to the AIA resolution with hmi_prep.

3 RESULTS

3.1 Flare Properties

Our multi-wavelength observations of AR 12087 detected an M3.9 flare on 2014 June 11. The *GOES* soft (1–8 Å) and hard (0.5–4.0 Å) X-rays peaked at 21:03 UT and rose by factors of 15 and 33 over the quiescent emission, respectively. The flare in the ROSA Mg light curve rose by a factor of 1.24 over the quiescent emission and peaked near 20:56:51 UT. The Ca K and Hα light curves increased by factors of 1.55 and 1.5 over their pre-flare, quiescent emission, respectively.

In Figure 3, we compare the narrow band filter data to those obtained from the *GOES* X-ray satellite. The rise time for the Mg flare was ∼105 s, with decay times of the narrow band filters exceeding 30 min and the overall emission staying larger than the pre-flare quiescent emission for the remaining time of our observations. The *GOES* peak flux for our M3.9 flares is $3.9 \times 10^{-5}\,\mathrm{W\,m^{-2}}$. This works out to a total energy in the 1.0 to 8.0 Å band of 1.1×10^{29} erg for the 17 min flare duration. We summarize the flare parameters in different bands in Table 1 extracted from the regions noted in Section 2.

Table 1 Light Curve Results

λ	Peak (UT)	Rise (min)	Decay (min)	Peak/Quiescent
G-band	No Flare	...	...	...
Ca K	20:56:49	∼1.5	>30	1.55
Mg	20:56:51	∼1.7	∼30	1.24
Hα	20:56:51	∼1.5	>35	1.50
SDO 304	20:56:43	∼2	∼46	4.3
SDO 1600	20:56:31	∼31	∼28	4.6
SDO 193[1]	21:02:42	∼7	∼28	3.4
SDO 211[1]	20:58:01	∼2	1.4	1.7
SDO 335[1]	20:56:51	∼2	∼1.5	2.3
SDO 94[1]	21:04:25	∼9	∼33	12.7
SDO 131[1]	21:03:32	∼8	∼29	22
Hard X-Ray	21:03	∼10	∼17	33
Soft X-Ray	21:03	∼10	∼19	15

Notes: [1] Flare peaks occur several minutes later, consistent with "euv late phase" emission (see text).

3.2 Flare Morphology

The flare emerged in the Ca K, Mg and Hα images as two separate flare ribbons that evolved into a lower longer flare ribbon ("main" or "lower") with a length of about 25 Mm and a smaller sympathetic flare ribbon ("upper") about 18 Mm long separated above by 7 to 10 Mm. We looked for differences in the flare properties across the flare ribbons in different regions. We show the flare light curves extracted in all three bands from these different regions in Figure 4(a) along with the flare image for Hα. A movie of the Hα images during the flare is also linked to Figure 4(a). There was essentially no difference in the rise times between the east and west regions surrounding the lower main flare ribbon. Moving from east to west along the lower flare ribbon reveals similar rise times, with the largest peak from the region labeled with box "5". Although in the main flare ribbons, the left region (box labeled "0") rises about 30 seconds before the emission from the upper (sympathetic) flare ribbon (labeled box "7"). The ribbon appears to be erupting along the east-to-west direction, but not in a linear fashion that makes a propagation velocity easily calculated. The more eastward and westward regions showed a more gradual increase than the central regions and only reached a level ≈1.5 times higher than the quiescent emission, about 40% lower than the flare peaks for the central regions of the main flare ribbon. In the next section we investigate velocities using time-distance techniques.

3.3 Velocities

We attempted to measure the propagation speed of the erupting ribbons in the photosphere and chromosphere during the flare's evolution in the narrow filter bands (Ca K, Mg and Hα) using time-distance techniques. Although it is difficult to distinguish a propagation velocity across the flare ribbon, we find a velocity of $\approx 60\,\mathrm{km\,s^{-1}}$ (shown in Fig. 4b) for the expansion at the western end of the main flare ribbon in both Hα and Ca K. Similar velocities were identified for the Mg band, but were difficult to derive based on its longer cadence, and lower contrast and signal-to-noise. These velocities compare well with previous studies. Huang et al. (2014) found velocities of fil-

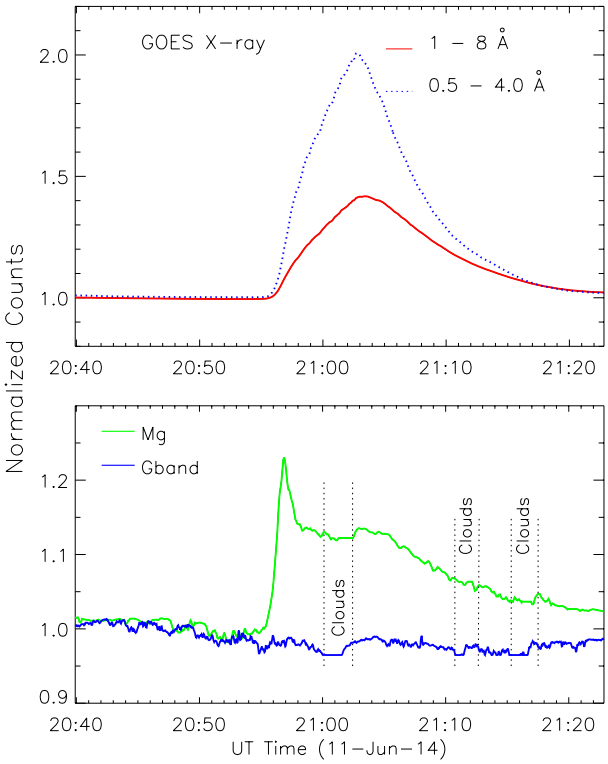

Fig. 3 Sample light curves for the 2014 June 11 M3.9 flare as a function UT times on 2014 June 11 . The top panel shows both the *GOES* soft X-ray channels with the 0.5 – 4 Å displayed in *blue* and the 1.0 – 8.0 Å in *red*. The lower panel depicts the ROSA Mg (*green*) and G-band (*blue*) light curves. Intervals disrupted by clouds are indicated in the lower panel.

ament eruptions observed in Hα up to 85 km s^{-1}. More puzzling are smaller features moving as fast as 300 km s^{-1} (blue and orange arrows in Fig. 4(b)). These large velocities (over 200 km s^{-1}) in an expanding ribbon are unusual, and are most likely associated with erupting filaments. Such large velocities of 340 km s^{-1} and up to 400 km s^{-1} were observed in a filament eruption in the *SDO* 304, 171 and 193 Å bands by Zhu et al. (2015).

4 DISCUSSION

We investigated the properties of an M3.9 flare by observing in multiple narrow and continuum band filters, and supplemented with EUV imaging data from *SDO*. Many issues still remain in our understanding of the details of flare physics (densities, temperatures and magnetic field configurations) that can only be derived from simultaneous observations at high temporal resolution of many layers in the solar atmosphere.

4.1 Flare Properties

We observed intensity increases ≈120% to 150% in the Mg, Ca K and Hα narrow band filters during the flare. Intensity increases for the flare observed in the *SDO* EUV were several times larger and the *GOES* X-rays increased by a factor of 15 in the soft X-ray band and over a factor of 30 for the harder band. These observed intensity increases in our narrow band filter are slightly lower than those of previous studies (Keys et al. 2011) and may indicate the majority of the flare emission is at hotter temperatures, as observed by the factor of 4–5 times increase observed with *SDO*.

4.2 Flare Morphology

Our observations covered nearly 1 hour before the flare and we are able to observe the detailed morphology of the flare ribbons change on a timescale of seconds. We classify this as a two-ribbon flare showing a lower larger "main" ribbon and an upper smaller region observed in our Ca K, Mg and Hα flare emission. Similar flare morphology was observed by Brannon et al. (2015) using *Interface Region Imaging Spectrograph* (*IRIS*) and *SDO* observations of an M-class flare. These ribbons of our flare appear to be related and occur within 30 s of each other. We find a length of ≈25 Mm for the lower main flare ribbon in Hα, Ca K and Mg bands. The flare ribbons are very similar to those of white-light flare emitting regions (Svestka 1976; Dodson-Prince & Bruzek 1977) and can be compared in our Mg

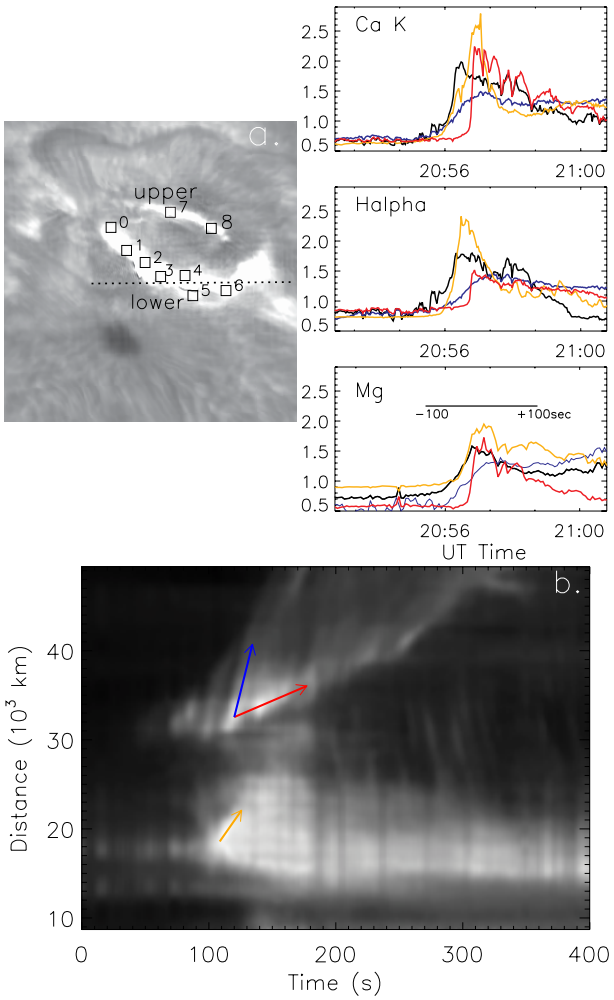

Fig. 4 Shown are comparisons of the Hα, Ca K and Mg light curves extracted from different spatial regions during the M3.9 flare and a time-distance plot for Hα. (a) (*upper panels*) The regions from which the light curves were extracted are shown in the left upper panel for Hα only. The *dashed horizontal line* marks where the time-distance plot was taken. The upper left panels display light curves extracted from four selected regions (0 – *black*, 3 – *blue*, 5 – *orange*, 7 – *red*, for ease of presentation), from top to bottom for: Ca K, Hα and Mg, respectively. (b) (*lower panel*) Time-distance plot showing motion along the upper and lower flare ribbons for Hα. The velocity derived for the western edge of the main ribbon of $\approx$60 km s^{-1} is indicated with the *red arrow*, and higher velocities of $\approx$300 km s^{-1} for smaller expanding regions are signified with the *blue arrow*. The derived velocities in the lower ribbon of $\approx$250 km s^{-1} are also depicted with the *orange arrow*. A movie of the HARDCam Hα images for Fig. 4(a) is available at *http://www.raa-journal.org/docs/Supp/msRAA-2018-0310movie.mp4*. The movie starts at 20:55:30 and is shown at a rate of 1 frame per second. The first and last frames are labeled.

band to the Mg observations of Lawrence et al. (1983), albeit the 1983 data are at lower spatial resolution.

4.3 Velocities

We find almost no difference in the flare's rise times for light curves extracted from regions across the main flare ribbon (Fig. 4(a)) and velocities when comparing various physical regions of the flare using time-distance plots. Also, the rise and decay times between these regions are all very similar (see Fig. 4(a)). The peaks of the Mg, Ca K and Hα emission are all within $\approx$ 2 s (Fig. 5). Typical formation heights for Ca K and Hα are 1300 km and 1500 km, respectively (Vernazza et al. 1981; Fontenla et al. 1990). This would imply a propagation velocity of about 100 km s^{-1} between these two layers, but the uncertainties are large. However, it is curious that the Mg emission, which forms near 700 km (Schmieder 1979) occurs within seconds of the Ca K and Hα emission peaks. This implies that, during the flare, this emission could be formed at greater heights, similar to the Ca K and Hα formation heights. This would be in agreement with flaring models presented by Mauas et al. (1990). This discrepancy may also result from the width of the Mg filter being sensitive to emission at several depths, and we also realize the formation heights of chro-

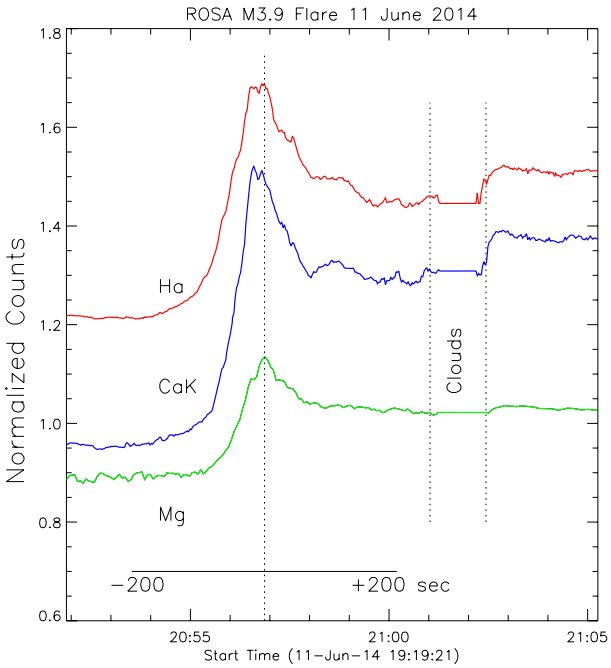

Fig. 5 Light curves from different filters for the M3.9 flare. From top to bottom are the Hα (*red*), Ca K (*blue*) and Mg (*green*) cases plotted in normalized counts (Mg is offset for ease of presentation). No significant delay in the flare peak times is observed between the Ca K and Hα, and between these two bands and Mg, and is indicated with a *vertical dashed line* in addition to an interval affected by clouds (see text).

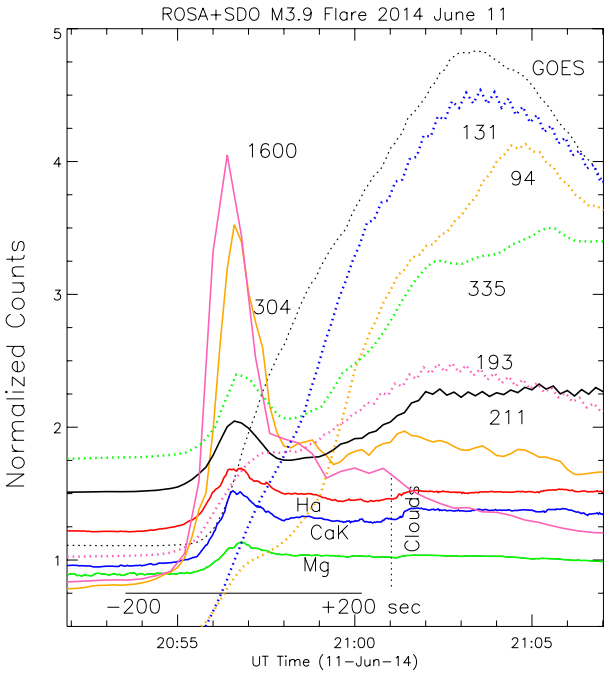

Fig. 6 Plotted are the light curves for the cooler (193, 211, 304 and 1600 Å) and hotter (94, 131, and 335 Å) *SDO* channels, the *GOES* soft X-ray band (1–8 Å; SXR), and our Ca K (*blue solid line*), Mg (*green solid line*) and Hα (*red solid line*) narrow band filter data. The *SDO* AIA channels shown are: 304 (*orange solid line*), 1600 (*pink solid line*), 211 (*black solid line*), 193 (*pink dotted line*), 335 (*green dotted line*), 94 (*orange dotted line*) and 131 Å (*blue dotted line*). Individual light curves are normalized by their average counts and are offset for ease of presentation. The re-scaled *GOES* soft X-ray band (SXR; 1.0 – 8.0 Å) is overplotted (*black*, *dotted line*) and aligns with the "euv late-phase" emission (see text).

mospheric spectral lines during the flare are significantly different than when comparing to the VAL model for the quiet Sun.

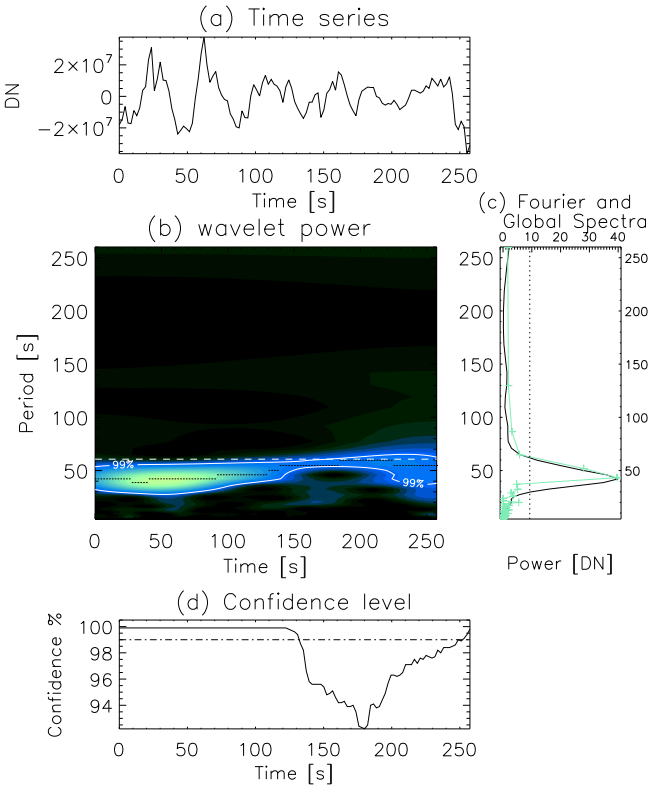

Fig. 7 Temporal analysis of the de-trended Hα filter light curve as discussed in Sect. 4.4. (a) The top panel displays the original Hα light curve for ≈4 min after the flare peak. (b) The wavelet power transform along with locations where detected power is at, or above, the 99% confidence level is contained within the contours. (c) The right-hand plot shows the summation of the wavelet power transform over time (*solid line*) and the Fast Fourier power spectrum (*crosses*) over time, plotted as a function of period. Both methods indicate marginal detections in the 40−60 sec range. The global wavelet (*dotted line*) and Fourier (*dashed dotted line*) 95% significance levels are also plotted. The bottom panel, (d), depicts the probability levels ($p \times 100$), which are related to the percentage confidence attributed to the peak power at every time step in the wavelet transform.

Similar calculations can be carried out for the *SDO* data, although we caution that the 12 sec cadence of the AIA EUV channels and the 24 sec cadence of the 1600 Å channel make the uncertainties in these velocities large, and the *SDO* filters AIA filters are broadband, capturing emissions from multiple thermal layers with uncertain formation heights. However, this approach gives us a ballpark estimate for propagation velocities to compare with the photosphere and chromosphere. We use Reznikova et al. (2012) for *SDO*'s formation heights and find velocities consistent with $\sim$100 km s^{-1} between emission observed in the *SDO* 304 and 1600 Å channels (formation heights for *SDO* 304 and 1600 Å are 2200 km and 500 km, respectively), and for propagation between the 304 and *SDO* 171 (ΔH =1000 km). We can also compare our photospheric and chromospheric measurements to those of the transition region and corona as measured by *SDO*. We can compare the delay between Ca K and the *SDO* 304 Å band. These two layers have a height difference of 900 km for the standard VAL model and this results in a velocity of 75 km s^{-1}. If the Ca K formation height is much lower, i.e. 500 km, then the propagation velocity is larger, at ≈140 km s^{-1}, a slightly higher velocity than a typical M-class flare, and similar to velocities found for other *SDO* channels. Again we caution the quiet-Sun VAL model is not applicable for the formation heights of chromospheric spectral lines during the flare. The colder *SDO* channel (*SDO* 304 with about 50 000 K) had a longer decay time than a hot *SDO* channel (*SDO* 193 with about 1 million K), and, as we would have expected, the *SDO* 193 flare peaks much later (up to 6 min) than *SDO* 304, since *SDO* 193 covers the coronal region and *SDO* 304 the chromosphere. In Figure 6, we illustrate the light curves for several *SDO* channels along with our ground-based narrow band channels.

The later emission of the *SDO* 193 ($\approx 1.5 \times 10^6$ K) and 211 Å channels ($\approx 2 \times 10^6$ K), and the delays observed in the hotter channels (94 and 131 Å) peak up to 8 min later than the cooler *SDO* channels (e.g. 1600 and 304 Å). These later peaks can be attributed to the "euv late phase" as described in Woods et al. (2011) and Liu et al. (2013a). This emission may be caused by different higher, but connected, loops that have a different thermal history.

Figure 6 also includes the light curve for the 335 Å emission that traces Fe XVI at $\approx 2.5 \times 10^6$ for comparison to these works. Similar delays for the hotter *SDO* channels were observed by Cheng et al. (2015) for a two-ribbon M-class flare, a sample of flares presented by Aschwanden & Shimizu (2013) and the X-class flare observed by Liu et al. (2014). We also note that the *GOES* bands peaking several minutes later than the narrow band filters and cooler *SDO* channels are unusual. The *GOES* 1–8 Å soft X-ray (SXR) light curve is overplotted in Figure 6 and more closely aligns with the *SDO* 335, 94 and 131 Å channels and the "euv late-phase" emission. Such behavior of the *GOES* SXR flux lagging emission from the lower solar atmosphere has been witnessed before for between it and the *Transition Region and Coronal Explorer* (*TRACE*) 1600 Å emission for an M8.0 flare observed by Liu et al. (2013b), *SDO* 1600 Å emission for a C3.2 flare observed by Qiu et al. (2013) and with the Hα emission for a C4.1 flare observed by Deng et al. (2013). The early impulsive phase of our M3.9 flare observed in narrow band filters (Ca K, Hα, Mg) and cooler *SDO* bands (304 and 1600 Å) is readily attributed to rapid heating by non-thermal electron beam precipitation, however the lagging SXR flux is harder to explain.

Liu et al. (2013b), using an 0D EBTEL model, invoke continuously expanding ribbons, emitting in the UV that create new flare loops by continuous magnetic reconnection and continue to heat the corona. Qiu et al. (2013) call upon the cooling of hot plasma that has been evaporated into the corona to explain this later phase. The *GOES* SXR is sensitive to temperatures over 5 MK ($\log T = 6.7$) and its later peak agrees well with those observed in the *SDO* 94, 131 and 335 Å bands, which are sensitive to emission at temperatures greater than 2.5 MK ($\log T \approx 6.4$). Future X-ray solar flare observations need to include high spatial and temporal resolution of the lower solar atmosphere to better model such flare behavior.

4.4 Search for Quasi-periodic Pulsations

We searched for QPPs in our narrow band filter data using wavelet and Fourier techniques described in Jess et al. (2008b). We identified a suggested QPP with periods in the 40–60 s range for the Ca K, Mg and Hα bands. We present the results of this analysis in Figure 7 for Hα (selected from the largest region used in the other analysis for maximum signal-to-noise, although similar periods are derived for the smaller regions shown in Fig. 4(a)), including the de-trended light curve, wavelet and Fourier power, and confidence level. No detections of white light QPP have been found in solar flares and QPP in narrow band filters have only been suggested. QPPs of about 60 s were located after a C-class flare as reported by Keys et al. (2011), and more recently, Kolotkov et al. (2015) found quasi-harmonic behavior of QPP observed in an X3.2 flare with intrinsic modes in the 15 to 100 s range, and Brannon et al. (2015) identified periods of ≈140 s in an M-class flare. The mechanism for QPP is still currently under debate, but involves some form of oscillatory reconnection in the magnetic loops or in magnetohydrodynamics (MHD) modes (McLaughlin et al. 2012). More recently, quasi-period slipping was observed during an X-class flare using *IRIS* and *SDO* data (Li & Zhang 2015). The associated periods were found in the range of 3 to 6 min and attributed to tearing mode instability generating oscillatory reconnection that may ultimately be driven by solar p-modes.

5 SUMMARY AND CONCLUSIONS

We have presented multi-wavelength observations of the 2014 June 11 M3.9 flare. We observed intensity increases of ≈120%–150% in the Mg, Ca K and Hα narrow band filters during the flare. Intensity increases for the flare observed in the *SDO* EUV were several times larger (≈4 times for 304 Å with $T \approx 50\,000$ K), and the *GOES* X-rays increased over factors of 15 and 33 for the soft and hard bands, respectively. The flare morphology observed in these narrow band filters shows a main flare ribbon and a sympathetic flare ribbon about 7 to 10 Mm away. Only modest delays are identified between the onset of emission across the main flare ribbon and up to 30 s between the main flare regions and of the nearby sympathetic flare (upper region). The peak flare emission occurs within a few seconds for the Ca K, Mg, and Hα bands. Time-distance techniques find propagation velocities of $\approx 60\,\mathrm{km\,s^{-1}}$ for the main flare ribbon and velocities as high as $300\,\mathrm{km\,s^{-1}}$ in smaller regions of the main flare ribbon that we attribute to filament eruptions. Propagation velocities between the chromosphere and coronal layers, although uncertain, are found to be as large as $\approx 100\,\mathrm{km\,s^{-1}}$. These results and delays and velocities for different coronal heights observed with *SDO* are consistent with this velocity, and agree well with the simple model of energy propagation versus height, although a more detailed model for the flaring solar atmosphere is needed. Hotter *SDO* channels exhibit emission with delays of up to 8 min and are consistent with the "euv late phase" observed for several M- and X- class flares. Finally, we detected marginal QPPs in the 40–60 s range for the Ca K, Mg and Hα bands, and such measurements are currently lacking in the literature, but are important for

disentangling the detailed flare-physics. Future high time resolution observations of solar flares (such as those available with DKIST) are important for disentangling the detailed flare-physics.

Acknowledgements We thank the NSO Dunn Solar Telescope staff, including Doug Gilliam, for their excellent support of this project, and we dedicate this paper to the late Michael Bradford whose keen eye pointed out this solar flare. The work of D.K. was supported by Sêr Cymru II Part-funded by the European Regional Development Fund through the Welsh Government. D.K. acknowledges support from the Georgian Shota Rustaveli National Science Foundation project FR17_323. We thank an anonymous referee for suggested improvements to the manuscript.

References

Aschwanden, M. J., & Shimizu, T. 2013, ApJ, 776, 132
Bai, X.-Y., Deng, Y.-Y., Su, J.-T., et al. 2014, RAA (Research in Astronomy and Astrophysics), 14, 193
Brannon, S. R., Longcope, D. W., & Qiu, J. 2015, ApJ, 810, 4
Cavallini, F. 2006, Sol. Phys., 236, 415
Cheng, X., Hao, Q., Ding, M. D., et al. 2015, ApJ, 809, 46
Deng, N., Tritschler, A., Jing, J., et al. 2013, ApJ, 769, 112
Dodson-Prince, H. W., & Bruzek, A. 1977, in Astrophysics and Space Science Library, 69, Illustrated Glossary for Solar and Solar-Terrestrial Physics, eds. A. Bruzek, & C. J. Durrant, 81
Fletcher, L., Dennis, B. R., Hudson, H. S., et al. 2011, Space Sci. Rev., 159, 19
Fontenla, J. M., Avrett, E. H., & Loeser, R. 1990, ApJ, 355, 700 (FAL90
Grant, S. D. T., Jess, D. B., Moreels, M. G., et al. 2015, ApJ, 806, 132
Huang, Z., Madjarska, M. S., Koleva, K., et al. 2014, A&A, 566, A148
Hudson, H. S. 2011, Space Sci. Rev., 158, 5
Hudson, H. S., Wolfson, C. J., & Metcalf, T. R. 2006, Sol. Phys., 234, 79
Isobe, H., Kubo, M., Minoshima, T., et al. 2007, PASJ, 59, S807
Jess, D. B., Mathioudakis, M., Crockett, P. J., & Keenan, F. P. 2008a, ApJ, 688, L119
Jess, D. B., Mathioudakis, M., Erdélyi, R., et al. 2008b, ApJ, 680, 1523
Jess, D. B., Mathioudakis, M., Christian, D. J., et al. 2010, Sol. Phys., 261, 363
Jess, D. B., De Moortel, I., Mathioudakis, M., et al. 2012, ApJ, 757, 160
Jess, D. B., Dillon, C. J., Kirk, M. S., et al. 2018, arXiv:1812.06978
Keys, P. H., Jess, D. B., Mathioudakis, M., et al. 2011, A&A, 529, A127
Kolotkov, D. Y., Nakariakov, V. M., Kupriyanova, E. G., et al. 2015, A&A, 574, A53
Kuridze, D., Mathioudakis, M., Simões, P. J. A., et al. 2015, ApJ, 813, 125
Kuridze, D., Mathioudakis, M., Christian, D. J., et al. 2016, ApJ, 832, 147
Lawrence, J. K., Chapman, G. A., & Herzog, A. D. 1983, Sol. Phys., 89, 341
Lemen, J. R., Title, A. M., Akin, D. J., et al. 2012, Sol. Phys., 275, 17
Li, T., & Zhang, J. 2015, ApJ, 804, L8
Liu, K., Zhang, J., Wang, Y., et al. 2013a, ApJ, 768, 150
Liu, W.-J., Qiu, J., Longcope, D. W., et al. 2013b, ApJ, 770, 111
Liu, R., Titov, V. S., Gou, T., et al. 2014, ApJ, 790, 8
Mauas, P. J. D., Machado, M. E., & Avrett, E. H. 1990, ApJ, 360, 715
McLaughlin, J. A., Thurgood, J. O., & MacTaggart, D. 2012, A&A, 548, A98
Milligan, R. O. 2015, Sol. Phys., 290, 3399
Milligan, R. O., Gallagher, P. T., Mathioudakis, M., et al. 2006, ApJ, 638, L117
Neidig, D. F. 1989, Sol. Phys., 121, 261
Pevtsov, A. A., Balasubramaniam, K. S., & Hock, R. A. 2007, Advances in Space Research, 39, 1781
Qiu, J., Sturrock, Z., Longcope, D. W., et al. 2013, ApJ, 774, 14
Reardon, K. P., & Cavallini, F. 2008, A&A, 481, 897
Reznikova, V. E., Shibasaki, K., Sych, R. A., et al. 2012, ApJ, 746, 119
Rimmele, T. R. 2004, in Proc. SPIE, 5490, Advancements in Adaptive Optics, eds. D. Bonaccini Calia, B. L. Ellerbroek, & R. Ragazzoni, 34
Scherrer, P. H., Schou, J., Bush, R. I., et al. 2012, Sol. Phys., 275, 207
Schmieder, B. 1979, A&A, 74, 273
Schou, J., Scherrer, P. H., Bush, R. I., et al. 2012, Sol. Phys., 275, 229
Svestka, Z. 1976, Solar Flares (Springer-Verlag Berlin Heidelberg)
Vernazza, J. E., Avrett, E. H., & Loeser, R. 1981, ApJS, 45, 635 (VAL)
Wöger, F., von der Lühe, O., & Reardon, K. 2008, A&A, 488, 375
Woods, T. N., Hock, R., Eparvier, F., et al. 2011, ApJ, 739, 59
Zhu, C., Liu, R., Alexander, D., et al. 2015, ApJ, 813, 60